DC Magnetic Field Based 3D Localization With Single Anchor Coil

Ryo Shirai, *Student Member, IEEE*, and Masanori Hashimoto, *Senior Member, IEEE*

***Abstract*—Indoor localization technologies are rapidly attracting attention in recent years since those are required by indoor navigation, IoT, smart city, etc. However, currently available indoor localization techniques, such as Wifi based method and multi-anchor based method, require high installation cost and have an insufficient robustness problem. This paper proposes a DC magnetic field based robust indoor 3D localization method with a single anchor coil. The proposed method estimates the sensor position from both geomagnetism and artificially generated DC magnetic field. The proposed method does not require any pre-measurement or multi-anchor nodes in the minimal configuration, and hence it can realize instant 3D localization with lower installation cost. This work analyzed the magnetic field generated by a coil both with numerical simulation and prototyped sensor node. We experimentally evaluated the proposed method supposing tabletop-scale and room-scale applications. For table-top scale applications, the proposed method estimates the 3D position with the maximum error of 6.5 mm in the range of 250 mm. For room-scale applications, which require coverage area expansion with multiple anchor coils, the proposed method localizes the sensor with the maximum error of 14.7 cm in 3.0 m × 1.5 m area.**

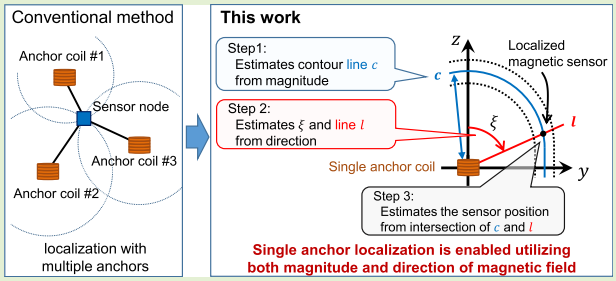

***Index Terms*—Indoor localization, coil, DC magnetic field, geomagnetic sensor, Internet of Things (IoT).**

I. Introduction

THANKS to continuous advances in VLSI scaling technology for several decades, implementing small volume sensor nodes has become possible. Small sensor nodes, such as sub-cm^3 ones, are applicable for many applications in the era of IoT since such tiny sensor nodes can be embedded into most of things around us and can be installed anywhere [1]. Consequently, information density around us is improved significantly, which is one of the expected characteristics contributing to improving our quality of life [2]. Besides, the information from sensor nodes, such as temperature, humidity, luminance, etc., gains its significance when it is associated with the position information of each sensor node. Motivated by this, location-based service (LBS) that combines sensor output and sensor position information has been studied extensively [3]. To realize LBS, establishing an accurate node localization method is indispensable.

Manuscript received November 17, 2019; accepted December 5, 2019. Date of publication December 23, 2019; date of current version March 5, 2020. This work was supported by the Japan Society for the Promotion of Science (JSPS) KAKENHI (Grant Number JP15H01679 and JP19J11322). The associate editor coordinating the review of this article and approving it for publication was Prof. Guiyun Tian. *(Corresponding author: Ryo Shirai.)*

The authors are with the Department of Information Systems Engineering, Osaka University, Suita 565-0871, Japan (e-mail: shirai.ryo@ist.osaka-u.ac.jp; hasimoto@ist.osaka-u.ac.jp).

Digital Object Identifier 10.1109/JSEN.2019.2961365

Sensor nodes for IoT applications can be installed both indoors and outdoors whereas, for particular applications, the sensor nodes tend to stay indoors or outdoors. For outdoor localization, research on GPS based localization method is actively conducted, e.g. [4]. Outdoor applications can often tolerate errors within a few meters. When using GPS, installing facilities dedicated to location estimation is unnecessary, and therefore it is suitable for most IoT applications. On the other hand, when it comes to indoor sensor nodes, localization is relatively difficult and then is not established. Since the GPS signal is damped severely in indoor environment, the sensor node is no longer able to utilize the GPS signal. Even if the sensor node catches the GPS signal, the error increases indoors and can be several meters. Nevertheless, the estimation accuracy required for indoor applications is extremely high compared to outdoor ones, and precision within 1 meter or less is usually demanded.

For these reasons, many methods using other signal sources than GPS have been proposed for indoor location estimation [5]. However, several problems remain in the existing methods, where the detail will be discussed in the next section. Some methods require multiple reference anchor nodes even with the minimal configuration, and consequently the installation cost can be large. Position estimation methods that require preliminary measurement are also being studied, but there is an inherent problem that those are vulnerable to environmental change. To solve these problems, this paper

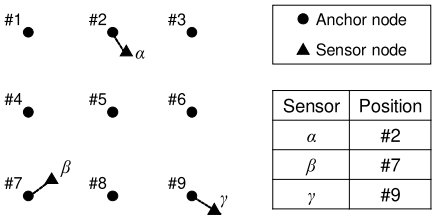

Sensor	Position
α	#2
β	#7
γ	#9

Fig. 1. Proximity based localization method.

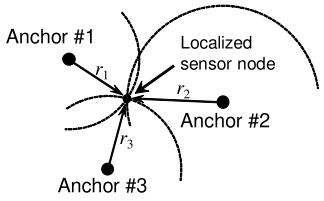

Fig. 2. Lateration based localization.

proposes a DC magnetic field based localization method that can estimate the position without preliminary measurement or multiple anchor nodes.

The rest of this paper is organized as follows. Section II introduces the related work on indoor localization. Section III analyzes artificial DC magnetic field which is obtained by numerical simulations. Section IV describes the proposed localization method which can estimate sensor position only with a single anchor coil. Section V shows the correlation between simulation and experimentation and presents localization results. Section VI discusses the localization error and the coverage area of the proposed method with single and multiple anchor nodes. Lastly, concluding remarks of this paper are given in Section VII.

II. Related Work

There are four popular ideas for indoor localization: proximity, fingerprint, camera and triangulation. Each idea utilizes a different type of signal or information. The following first explains each idea briefly and then introduces several methods based on each idea.

A. Proximity Based Methods

The proximity based method estimates the sensor position using pre-installed multiple anchor nodes. Fig. 1 exemplifies the proximity based method. The sensor node detects the nearest anchor node and sets the position of the anchor node as sensor node's own position as shown in the right bottom table in Fig. 1. Here, the location of all the anchor nodes in the system must be known beforehand.

In the proximity method, RFID and the like which is small enough and can be installed anywhere are used as the anchor node [6] since the position estimation accuracy highly depends on the density of anchor nodes and such small anchor nodes can be easily distributed densely. In this method, the position estimation accuracy improves as the density of the anchor nodes is intensified. On the other hand, there is a disadvantage that the installation cost is relatively high because the number of anchor nodes is quite large and their locations must be measured beforehand.

B. Fingerprint Based Methods

The fingerprint based method estimates the position by finding the most similar data from the previously measured data with the data presently acquired by the sensor node. Here, *fingerprint* means each location has unique measurement data, and the pairs of position information and measurement data are stored in Look Up Table (LUT).

Wi-Fi signal is often used for fingerprint based method [7], [8]. Wi-Fi localization is advantageous in terms of installation cost since it does not require new equipment dedicated for position estimation. On the other hand, the fingerprint method suffers from the disadvantage that the preliminary measurement is necessary to build a LUT. In many Wi-Fi based position estimation methods, site survey needs to be performed to construct the LUT every time the indoor environment changes, which results in high operation cost. To avoid this problem, Wu et al. propose a Wi-Fi based localization method that makes site survey omittable by using the information collected by smartphones for LUT update [9]. Another concern of the Wi-Fi based localization method is the risk of privacy being violated by man-in-the-middle attacks via the Wi-Fi network [10].

C. Camera Based Method

The camera based method utilizes image processing techniques, e.g. Hough transform and machine learning, to estimate object positions. In camera based localization, depth cameras are often used in addition to RGB cameras. Figueiredo et al. propose an RGB-D camera based localization method that estimates the position of daily items using Random Sample Consensus (RANSAC) and Hough transform [11]. The camera based method has an advantage that it does not require installation of multiple anchors or costly adjustment to cope with the environmental change. On the other hand, occlusion problems and privacy problems exist.

D. Triangulation Based Methods

Triangulation includes two methods: lateration and angulation. Fig. 2 illustrates lateration. The distance between the sensor node and the anchor node is obtained by, for example, time of flight (ToF) and received signal strength (RSS), and the position is identified with the distances to three anchor nodes. When there are more than three anchor nodes, redundant distance information can be used to mitigate the effect of measured distance error on the localization accuracy. Note that the anchor nodes are supposed to be accurately localized beforehand.

As a signal for distance estimation, magnetic field is often used [12]–[14]. Angelis et al. propose a position estimation method based on AC magnetic field [13]. There is an advantage that the coverage area is wide since AC magnetic field propagates farther than DC one. On the other hand, there is a disadvantage that the accuracy degrades when being affected by metallic objects. To overcome this problems, Blankenbach et al. study a DC magnetic field based localization [14]. The DC magnetic field based method is more robust

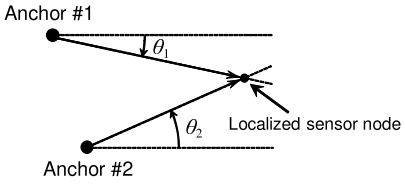

Fig. 3. Angulation based localization.

than the AC one since DC magnetic field can penetrate non-ferrous metallic material. However, it has a disadvantage that the coverage area is small.

Next, angulation is explained with Fig. 3. Angulation utilizes anchor-to-node relative angle information to localize the node whereas lateration utilizes node-to-anchor distance information. Angulation has an advantage that two anchor nodes are sufficient for positioning.

To further reduce the number of anchor nodes, Song et al. propose a hybrid method combining lateration and angulation, in which AC magnetic field is used for position estimation [15]. This hybrid method can estimate the sensor position with a single anchor coil by using the relative angle of the sensor viewed from the anchor in addition to the anchor-node distance information. The single anchor node brings the advantage of low installation cost and require no anchor localization. However, this method cannot be used in the environment including metallic objects since AC magnetic field cannot penetrate metal [13]. At the same time, this method is not suitable for small sensor nodes since each sensor node requires a complex structure coil.

In this paper, to resolve these problems, we develop a lateration-angulation hybrid localization method using DC magnetic field and single anchor coil. Both AC magnetic field based method and DC magnetic field based method utilize the magnitude and direction information of the magnetic field. To sense high frequency AC magnetic signals, however, the sensor node must be equipped with multiple coils with a large diameter, and therefore, an increase in the sensor node volume is inevitable and the AC magnetic field based method limits its application. On the other hand, the DC magnetic field based method, which we focuses on this paper, does not require a coil for the sensor node. The DC magnetic field can be sensed by a small MEMS (Micro Electro Mechanical Systems) geomagnetic sensor and can be a promising solution to actualize a small localizable sensor node.

III. Analysis of DC Magnetic Field

In this section, we analyze artificially generated DC magnetic field with a numerical integration simulator. First we introduce the equation for the single loop coil, and then, perform a simulation experiment with a general solenoid whose number of turns is more than one. The objective of this section is to illustrate the existence of a relationship between the position of the sensor node and magnetic field, which will be exploited by the proposed localization method in the next section.

First, we review the single loop coil placed on the xy plane in Fig. 4. In this figure, magnetic flux density vector $\mathbf{B}(r, \theta, \phi)$ generated at point $P(r, \theta, \phi)$ is given by the following

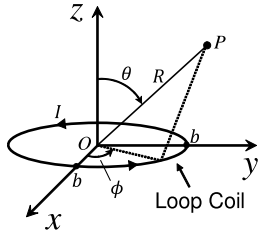

Fig. 4. Coordinate setting.

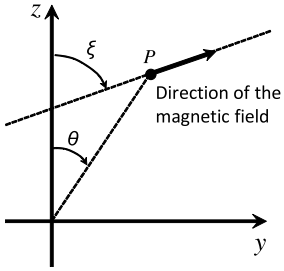

Fig. 5. Definition of ξ.

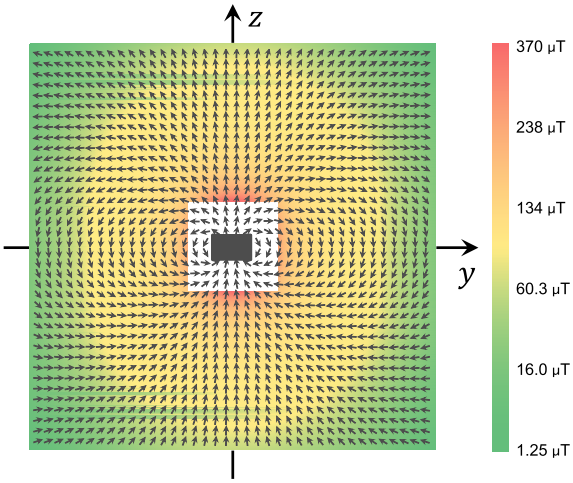

Fig. 6. Obtained heatmap of the magnitude and the plot of the direction of magnetic field generated by the solenoid ($I = 1$[A]). The intensity inside the white rectangle is omitted due to visibility reason.

equation [16]:

$$\mathbf{B} = \nabla \times \mathbf{e}_\phi \frac{\mu_0 I b}{2\pi} \int_{-\frac{\pi}{2}}^{\frac{\pi}{2}} \frac{\sin\phi'}{\sqrt{r^2 + b^2 - 2br\sin\theta\sin\phi'}} d\phi', \quad (1)$$

where $\mathbf{e}_\phi$ is a unit vector of the ϕ direction, ϕ' is an integral parameter, and μ_0 is a magnetic constant. We can obtain the intensity and direction of the magnetic field by solving Eq. (1) with numerical integration. Here, the direction of the magnetic field is represented by ξ, and it is defined in Fig. 5.

Next, we analyze the magnetic field generated by a solenoid whose number of turns is more than one. Basically, magnetic field generated by a solenoid can be calculated by superposing the analysis results for a single loop coil. The coil to be analyzed has almost the same specification as the coil which will be used in the experiment, and its size is ϕ42 mm $\times$ 30 mm and the number of turns is 240. We performed the numerical simulation supposing 1A current was injected to the coil. Fig. 6 shows the magnitude and direction of the magnetic field

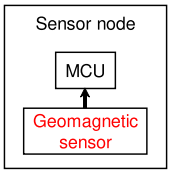

Fig. 7. Structure of the sensor node.

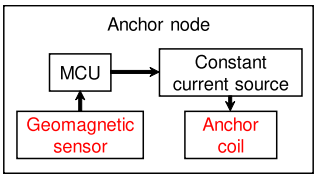

Fig. 8. Structure of the anchor node.

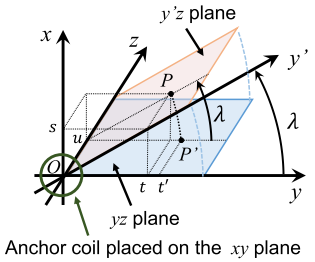

Fig. 9. Coordinate setting and definition of s, t, u, t' and λ.

at each point on the yz plane. Note that when ϕ is $\pi/2$ and point P is distant enough from the coil, x-direction component of the magnetic field is zero [16]. Therefore, Fig 6 shows only the y and z direction component of the magnetic field. In Fig. 6, the intensity of the magnetic field at the points near the coil, which correspond to the white rectangle, is not plotted since it is too strong and it deteriorates the visibility of the heat map. Fig. 6 suggests a simple geometric relationship between the position of point P and the magnitude of the magnetic field at P. Fig. 6 also shows that the values of ξ on the radial line, i.e. at the points having the same θ, are almost the same. This relation will be derived in detail and exploited for localization in Section IV.

IV. Proposed Localization Method

This section proposes a 3D localization method that can estimate the sensor position utilizing a single anchor coil. Figs. 7 and 8 show the structure of the sensor node and the anchor node supposed in the proposed method, respectively. Both the sensor node and the anchor node are equipped with a geomagnetic sensor that can sense weak DC magnetic field. The anchor node also includes a constant current source and anchor coil.

Figs. 9 and 10 show the coordinate setting and definition of $s, t, u, t', \lambda(\pi/2 \leq \lambda \leq \pi/2)$, and $\theta(0 \leq \theta \leq \pi/2)$. In Fig. 9, yz plane is parallel to the ground and x axis represents the height of the system. The anchor node is installed at the origin $O(0,0,0)$ and the sensor node locates at point $P(s,t,u)$. Fig. 9 shows y' axis in addition to the xyz coordinate system. $y'z$ plane includes a sensor node P, and λ denotes the angle between y' and y axis. $P'(0,t',u)$ is a point on the yz plane,

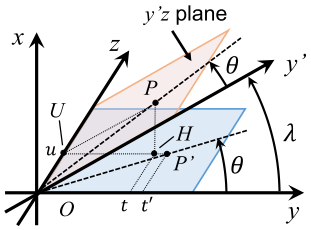

Fig. 10. Definition of θ.

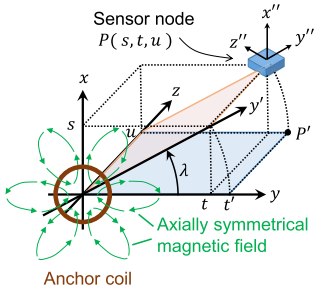

Fig. 11. xyz coordinate system is the absolute coordinate system and $xy'z$ coordinate system is utilized to calculate λ. The anchor coil placed on the origin is axially symmetric and hence the generated magnetic field is also axially symmetric. Therefore, we can estimate the magnetic field at the point P' from the magnetic field at point P.

and it is obtained by rotating the point P by λ [rad] around the z axis. Supposing t' is the y'-axis value of the point P, the following relationship is satisfied:

$$\overrightarrow{OP} = s\mathbf{e}_x + t\mathbf{e}_y + u\mathbf{e}_z = t'\mathbf{e}'_y + u\mathbf{e}_z, \tag{2}$$

where $\mathbf{e}_x, \mathbf{e}_y, \mathbf{e}_z$ and $\mathbf{e}'_y$ are unit vectors of x, y, z, and y' axis directions, respectively. θ in Fig. 10 represents the angle between line OP and y' axis, and it is equal to the angle between line OP' and y axis. The coordinates of points U and H are $U(0,0,u)$ and $H(0,t,u)$, respectively.

Section IV-A briefly explains the overview of the proposed localization method, and following sections from IV-B to IV-E focus on the detail of each localization step.

A. Overview

Our localization method estimates the three-dimensional position of sensor node P with the following four steps: posture estimation, altitude estimation, distance estimation, and angle estimation. Let us explain each step briefly before going into the details.

Fig. 11 illustrates two important coordinate systems utilized in the localization system. The sensor node is equipped with the tiny geomagnetic sensor and its coordinate system is depicted as $x''y''z''$ coordinate system. xyz coordinate system is the absolute coordinate system that is directly used for localization, i.e., the location in this coordinate system must be returned, and hence the data obtained by the sensor node should be based on this coordinate system. However, the magnetic field data observed by the sensor node are based on $x''y''z''$ coordinate system. Therefore, we have to perform coordinate transformation, and for this reason, we need to know the posture of the sensor node. In the posture estimation step, the sensor node estimates its facing direction by

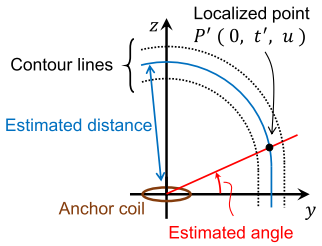

Fig. 12. Distance estimation and angle estimation step estimate the position of the point P' rather than the sensor node. These steps are conducted on yz plane. Each step draws the contour line and angle line according to the intensity and the direction of the magnetic field respectively, and then derive the position of P' by calculating the intercept point of those.

observing the geomagnetism and carries out the coordinate transformation of the measured data.

The position of P can be obtained by rotating P' by λ in Fig. 11 once λ and P' are obtained. Therefore, the remaining steps calculate λ and P'. The second altitude estimation step derives the value of λ. As discussed in Section III, the $x-$direction component of the magnetic field is zero. In addition to this, the magnetic field generated by the anchor coil is axially symmetrical to the z axis as shown in Fig. 11. By utilizing these two features, the system can derive the value of λ. Finally, the following two steps localize P'. The third distance estimation step estimates the distance between the anchor coil and point P' and calculates a contour line shown in Fig. 12. The final angle estimation step estimates the anchor-to-P' angle, and calculates an anchor-to-P' line as shown in Fig. 12. Using the anchor-to-P' distance and anchor-to-P' angle, P' is localized.

After the four steps, λ and the position of P' are available, and consequently P can be obtained. Following sections from IV-B to IV-E detail each step.

B. Posture Estimation

First, the proposed localization system estimates the posture of the sensor node P before starting position estimation. The posture of the sensor node P is estimated by the geomagnetism, which is the most common uniform magnetic field.

The posture of the sensor node is determined by the tilt angle and the horizontal rotation angle of the sensor node. In some indoor applications, the tilt angle is fixed since the objects with the sensor node are not placed arbitrarily. If it is not fixed, we measure the direction of the gravity with an acceleration sensor and estimate the tilt angle. The horizontal rotation angle is estimated with the direction of the geomagnetism. The following explains the estimation of the horizontal rotation angle.

Fig. 13 shows the definition of ψ, which corresponds to horizontal rotation angle. Fig. 13 also includes the coordinate system of the geomagnetic sensor embedded in the sensor node P, and it is defined by x'', y'', and z''. We regard as $y''z''$ plane is parallel to yz plane since the tilt angle of the sensor node is known and supposed to be already compensated. With this feature, as shown in Fig. 13, the coordinate system of the sensor node, i.e. $x''y''z''$ coordinate system, is rotated by ψ[rad] around the x axis from the coordinate system of the

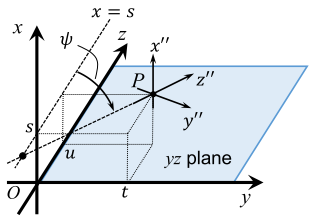

Fig. 13. The posture of the sensor node P.

anchor node, i.e. xyz coordinate system. Letting $\mathbf{B}_g$ denote the geomagnetism vector, the output of the geomagnetic sensor ($\mathbf{B}_{Pg} = (B_{Pgx''}, B_{Pgy''}, B_{Pgz''})$) in sensor node P satisfies the following equation.

$$\mathbf{B}_g = B_{Pgx''}\mathbf{e}''_x + B_{Pgy''}\mathbf{e}''_y + B_{Pgz''}\mathbf{e}''_z \tag{3}$$

where $\mathbf{e}''_x$, $\mathbf{e}''_y$, and $\mathbf{e}''_z$ are the unit vectors of x'', y'', and z'' axis directions, respectively. The geomagnetic vector is constant regardless of the observation location. Therefore, $\mathbf{B}_g$ can be also expressed as Eq.(4) using the output of the geomagnetic sensor ($\mathbf{B}_{Og} = (B_{Ogx}, B_{Ogy}, B_{Ogz})$) in the anchor node O.

$$\mathbf{B}_g = B_{Ogx}\mathbf{e}_x + B_{Ogy}\mathbf{e}_y + B_{Ogz}\mathbf{e}_z \tag{4}$$

Here, to simplify the discussion, we assume that y direction component of the geomagnetism is zero, which means B_{Ogy} is zero. Note that, on the other hand, this assumption is introduced only for simplifying the discussion, and the other situations can be discussed similarly. If we rotate vector $\mathbf{B}_{Pg}$ by $-\psi$[rad], it should match with vector $\mathbf{B}_{Og}$ since the geomagnetism can be regarded as almost equal at the locations of the anchor node and the sensor node. Therefore, we can obtain Eq.(5).

$$\begin{aligned}\begin{bmatrix} B_{Ogx} \\ 0 \\ B_{Ogz} \end{bmatrix} &= \begin{bmatrix} 1 & 0 & 0 \\ 0 & \cos -\psi & -\sin -\psi \\ 0 & \sin -\psi & \cos -\psi \end{bmatrix} \mathbf{B}_{Pg} \\ &= \begin{bmatrix} B_{Pgx''} \\ B_{Pgy''}\cos\psi + B_{Sz}\sin\psi \\ -B_{Pgy''}\sin\psi + B_{Sz}\cos\psi \end{bmatrix}\end{aligned} \tag{5}$$

From Eq. (5), we can obtain the relationship between ψ and $\mathbf{B}_{Pg}$ below.

$$\tan\psi = -\frac{B_{Pgz''}}{B_{Pgy''}} \tag{6}$$

Taking into account the range of $\tan^{-1}\left(-\frac{B_{Pgz''}}{B_{Pgy''}}\right)$ being limited to $-\pi/2 \le \tan^{-1}\left(-\frac{B_{Pgz''}}{B_{Pgy''}}\right)\psi \le \pi/2$, ψ is calculated as follows.

$$\psi = \begin{cases} \tan^{-1}\left(-\dfrac{B_{Pgz''}}{B_{Pgy''}}\right) & \text{if } B_{Pgz''} \ge 0, \\ \pi + \tan^{-1}\left(-\dfrac{B_{Pgz''}}{B_{Pgy''}}\right) & \text{otherwise.} \end{cases} \tag{7}$$

C. Altitude Estimation

This step first estimates λ to calculate s, which is the altitude of the sensor node P. Estimating λ requires the artificially generated magnetic field, and therefore the system gives

a constant current to the anchor coil. Here, we assume the output of the geomagnetic sensor mounted in the sensor node P is $\mathbf{B}_{P''e} = (B_{Pex''}, B_{Pey''}, B_{Pez''})$. To obtain the magnetic field vector generated by the anchor coil $\mathbf{B}_{P''}$, we subtract the geomagnetism $\mathbf{B}_{Pg}$ from $\mathbf{B}_{P''e}$ since $\mathbf{B}_{P''e}$ contains not only artificially generated magnetic field but also the geomagnetism.

$$\mathbf{B}_{P''} = \mathbf{B}_{P''e} - \mathbf{B}_{Pg} \tag{8}$$

We perform coordinate transformation using the obtained ψ and the rotation matrix since the coordinate system of $\mathbf{B}_{P''} = (B_{Px''}, B_{Py''}, B_{Pz''})$ is based on $x''y''z''$ coordinate system. $\mathbf{B}_P = (B_{Px}, B_{Py}, B_{Pz})$, which is based on xyz coordinate system after the transformation, can be expressed by Eq. (9).

$$\mathbf{B}_P = \begin{bmatrix} 1 & 0 & 0 \\ 0 & \cos -\psi & -\sin -\psi \\ 0 & \sin -\psi & \cos -\psi \end{bmatrix} \mathbf{B}_{P''} \tag{9}$$

The magnetic field generated by the anchor coil is axially symmetric around z axis since the anchor coil is placed at the origin on the xy plane and the central axis of the coil exactly accords with the z axis as illustrated in Fig. 11. Therefore, when we observe the magnetic field at the point P', $\mathbf{B}_{P'} = B_{P'x}\mathbf{e}_x + B_{P'y}\mathbf{e}_y + B_{P'z}\mathbf{e}_z$, $\mathbf{B}_{P'}$ can be calculated by rotating $\mathbf{B}_P$ by λ [rad].

$$\mathbf{B}_{P'} = \begin{bmatrix} \cos\lambda & -\sin\lambda & 0 \\ \sin\lambda & \cos\lambda & 0 \\ 0 & 0 & 1 \end{bmatrix} \mathbf{B}_P \tag{10}$$

As we discussed in the previous section, the x component of $\mathbf{B}_{P'}$ is zero since the point P' is on the yz plane.

$$\mathbf{B}_{P'} = \begin{bmatrix} 0 \\ B_{P'y} \\ B_{P'z} \end{bmatrix} \tag{11}$$

From Eqs. (10) and (11), Eq. (12) holds.

$$\begin{bmatrix} 0 \\ B_{P'y} \\ B_{P'z} \end{bmatrix} = \begin{bmatrix} B_{Px}\cos\lambda - B_{Py}\sin\lambda \\ B_{Px}\sin\lambda + B_{Py}\cos\lambda \\ B_{Pz} \end{bmatrix} \tag{12}$$

Then, we can derive λ from Eq. (12) as follows.

$$\lambda = \tan^{-1}\left(\frac{B_{Px}}{B_{Py}}\right) \tag{13}$$

Next, we calculate the altitude of the sensor node P, s, using λ. Focusing on $\triangle PUH$ in Fig. 10, the following relationship between s and λ is satisfied.

$$\sin\lambda = \frac{PH}{PU} = \frac{PH}{P'U} = \frac{s}{t'} \tag{14}$$

By arranging Eq. (14), we finally obtain s.

$$s = t'\sin\lambda \tag{15}$$

On the other hand, variable t' included in Eq. (15) is still unknown, and it will be calculated in the following steps.

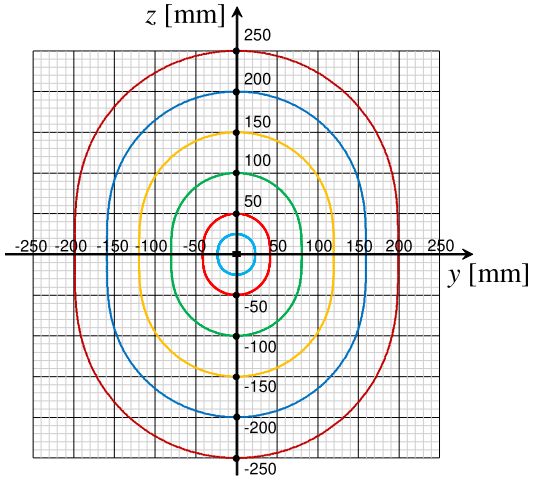

Fig. 14. Contour lines of the magnitude of magnetic field on yz plane.

D. Distance Estimation

We can estimate the position of the sensor node P by estimating the coordinate of point P' since the position of sensor node P can be obtained by rotating point P' by $-\lambda$ [rad] around the z axis. Therefore, the objective of the remaining two steps is to find the coordinate of point P'. In this step, we estimate the anchor-sensor distance from the magnitude of magnetic field generated by the anchor coil.

We can calculate the magnitude of the magnetic field using Eq. (16) since the generated magnetic field is axially symmetric around the z axis as shown in Fig. 11, and the magnitude at the point P' should be the same as that of at the sensor node P.

$$|\mathbf{B}_{P'}| = |\mathbf{B}_P| = \sqrt{{B_{Px}}^2 + {B_{Py}}^2 + {B_{Pz}}^2} \tag{16}$$

Fig. 6, which was introduced in Section III, shows the relationship between the position of the sensor node and the magnitude of the artificially generated magnetic field. Fig. 14 shows the corresponding contour map, where the contour lines go through $(0, 0, 25)$, $(0, 0, 50)$, $(0, 0, 100)$, $(0, 0, 150)$, $(0, 0, 200)$ or $(0, 0, 250)$. We can see that the contour line l that goes through point $(y, z) = (r_0, 0)$, where $r_0 > 0$, always passes the vicinity of point $(y, z) = (0, 5r_0/4)$ if r_0 is larger than 20 mm. Fig. 14 also indicates that the contour line l can be regarded as a straight line in the range of $0 \le z \le r_0/4$ and it can be approximated by the equation of a circle in the range of $z > r_0/4$. Therefore, we approximate contour line l with Eq. (17).

$$l : \begin{cases} y = r_0 & 0 \le z \le \dfrac{r_0}{4} \\ y^2 + \left(z - \dfrac{1}{4}r_0\right)^2 = r_0^2 & z > \dfrac{r_0}{4} \end{cases} \tag{17}$$

The error introduced by this approximation will be discussed in Section VI-A. Eq. (17) shows that, for any point on yz plane, we can find the point on y axis where the magnitude of the magnetic field is the same. Hence, if we have the relationship between the r_0, which is the y coordinate of the point Y on y axis, and the magnitude of the magnetic field at

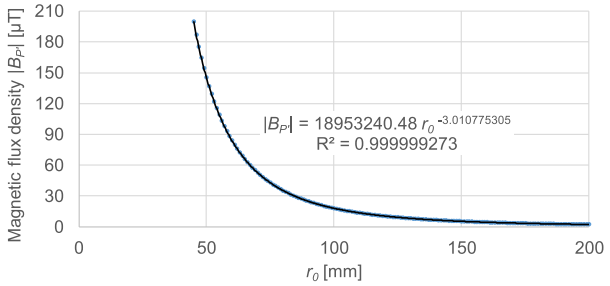

Fig. 15. Relationship between $|\mathbf{B}_{P'}|$ and r_0.

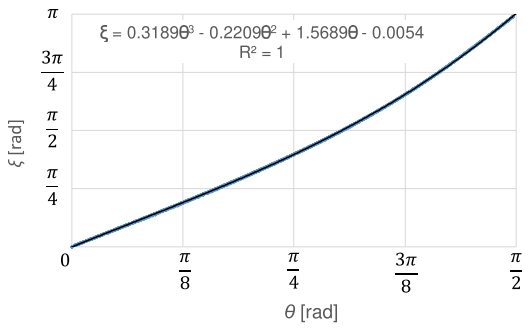

Fig. 16. Relationship between θ and ξ.

the point Y, we can estimate the magnitude at any point on yz plane.

Fig. 15 shows the relationship between r_0 and the magnitude, which is obtained by numerical simulation. Fig. 15 indicates that the magnitude of the magnetic field is proportional to r_0^{-3}. The inverse function of the equation in Fig. 15 is

$$r_0 = 261.3439338\ |\mathbf{B}_{P'}|^{-0.332140362}. \tag{18}$$

Let us summarize this step. Now, given $\mathbf{B}_{P'}$, we can obtain the equation of contour line l that goes through point $P'(0, t', u)$ with Eqs. (16), (17), and (18), and consequently anchor-sensor distance estimation is done. The next final step identifies the location on the contour line.

E. Angle Estimation

This step estimates the anchor-node angle θ and find the exact position of P' on contour line l. We can express the magnetic field ($\mathbf{B}_{P'}$) at the point P' with $\mathbf{B}_P$ using Eq. (12).

$$\mathbf{B}_{P'} = \begin{bmatrix} 0 \\ B_{Px}\sin\lambda + B_{Py}\cos\lambda \\ B_{Pz} \end{bmatrix} \tag{19}$$

We want to know ξ in Fig. 5 for the localization, and it is expressed by

$$\begin{aligned} \xi &= \frac{\pi}{2} - \tan^{-1}\frac{B_{P'z}}{B_{P'y}} \\ &= \frac{\pi}{2} - \tan^{-1}\left(\frac{B_{Pz}}{B_{Px}\sin\lambda + B_{Py}\cos\lambda}\right). \end{aligned} \tag{20}$$

Fig. 6 suggests the existence of the simple equation between ξ and θ. Fig. 16, which is calculated with numerical simulation, shows the relationship between θ and ξ indicating that ξ can be approximated by a cubic polynomial expression of θ. The inverse function of the equation in Fig. 16 becomes

$$\theta = -0.0008861\xi^3 - 0.06755\xi^2 + 0.7200\xi - 0.007633. \tag{21}$$

We can estimate the anchor-sensor angle θ using Eqs. (20) and (21). We can also obtain the equation of the straight line m that contains point P' with the obtained θ.

$$m:\ z = \tan\left(\frac{\pi}{2} - \theta\right) y \tag{22}$$

Both contour line l and straight line m should contain point P', and hence we can derive the coordinate of point $P'(0, t', u)$ just by calculating the intersection of the two lines as depicted in Fig. 12. The obtained u is z coordinate of not only the point P' but also the sensor node P. The obtained t' is used to estimate t, which is the y coordinate of the sensor node P, in the following procedure. We obtain the relationship among t, t' and λ focusing on $\triangle PUH$ in Fig. 10.

$$\cos\lambda = \frac{UH}{PU} = \frac{UH}{P'U} = \frac{t}{t'} \tag{23}$$

We obtain the relationship between t and t' by transforming Eq. (23) and can estimate the y coordinate of sensor node P.

$$t = t'\cos\lambda \tag{24}$$

Now, we successfully estimate the position of the sensor node $P(s, t, u)$ through the four steps: posture estimation, altitude estimation, distance estimation, and angle estimation. Here, let us mention the limitation of the proposed method. We need to set a constraint on the localizable angle since the directions of magnetic field at two points which are located point-symmetric to the center of the coil are identical and hence they cannot be distinguished. We call this unlocalizable area as dead-zone where the angle estimation step cannot work correctly. However, this dead-zone is not a serious problem in terms of the localization since we can minimize the effect of this dead-zone by choosing the anchor position carefully. The localizable angle can be any consecutive 180 degree in the range of 360 degree around the anchor coil. In other words, users can choose the localizable angle as they want, which contributes to a high degree of freedom in the installation direction of the anchor node and mitigates the effect of the dead-zone. Even when the situation that the coverage area is too small due to this dead-zone, we can expand the coverage area by introducing multiple anchor coils as we will discuss in Section VI-D.

V. Evaluation

This section presents measurement results obtained with a prototyped system to validate the proposed localization method. Section V-A introduces experimental conditions and environment. In Section V-B, we measure the geomagnetism with a geomagnetic sensor and show the performance of the direction estimation based on the geomagnetism only. Next, in Section V-C, we evaluate the artificially generated DC magnetic field with the geomagnetic sensor and verify the correlation between simulation and measurement results. Section V-D shows 3D localization results with the proposed

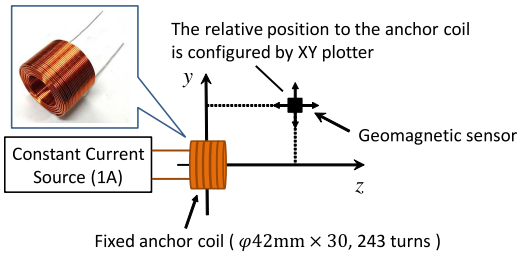

Fig. 17. Positional relationship between the anchor coil and the sensor node.

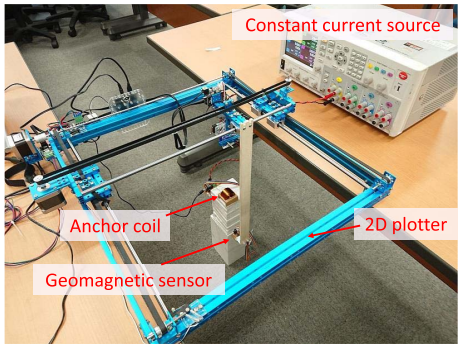

Fig. 18. Photo of the measurement environment.

localization method using prototyped sensor and anchor nodes, and Section V-E experimentally demonstrates the proposed method is not sensitive to non-ferrous metal.

A. Setup

Fig. 17 explains the experimental environment, and Fig. 18 shows the photo of the actual environment. An anchor coil is fixed at the origin of the coordinate system as shown in Fig. 17. The size of the anchor coil is $\phi 42$ mm$\times$30 mm and the number of turns is 243. We evaluate the outputs of a geomagnetic sensor (LIS3MDL) that is fixed to a 2D plotter in Fig. 18. The installed 2D plotter is responsible for positioning the geomagnetic sensor. We can change the position of the geomagnetic sensor in the yz plane in Fig. 9 by sending specific commands to the 2D plotter.

B. Geomagnetism Based Posture Estimation

We first estimate the posture of the geomagnetic sensor using the geomagnetism only. Here, the posture of the sensor node ψ is defined by the angle difference between the anchor coil and the geomagnetic sensor. This posture estimation procedure is performed with Eq. (7) and outputs of the geomagnetic sensor according to the discussion in Section IV-B.

Fig. 19 shows the result of the posture estimation when the angle difference between the geomagnetic sensor and the anchor node is varied from -90 to 90 degree. Here, each posture estimation is performed using 10 samples of the sensor output. Error bars in Fig. 19 denote the standard deviation that was obtained by 100 experiments each. The mean angle error is 0.88 degree and the maximum estimation error is 2.43 degree, which indicates that the geomagnetic sensor has sufficient accuracy and the system can estimate the posture of the sensor node precisely. With this posture information,

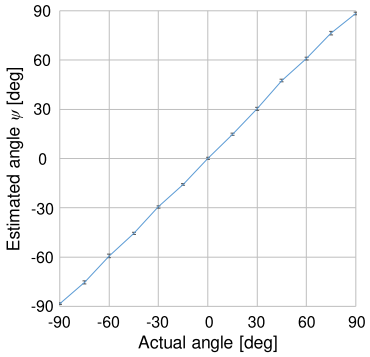

Fig. 19. Evaluation result of posture estimation.

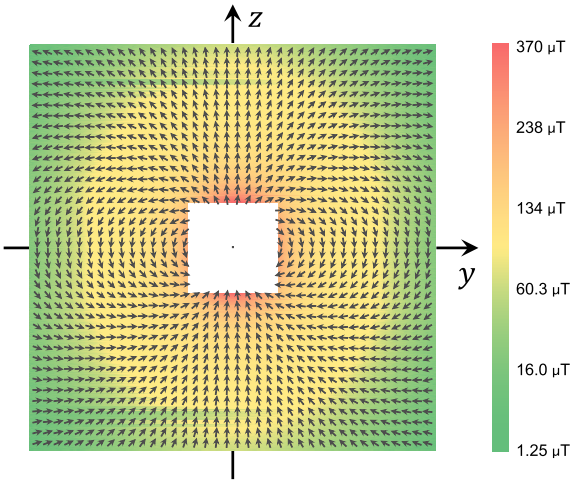

Fig. 20. Measured magnitude and direction of the magnetic field.

we can convert the coordinate system of the sensor node into the anchor node's one using Eq. (9) even when the geomagnetic sensor and the anchor coil do not face in the same direction.

C. Artificially Generated Magnetic Field

Next, we measure the DC magnetic field generated by the anchor coil to which 1A current is given. We sweep the sensor position on yz plane in the range of 400 mm $\times$ 400 mm with 1 mm interval using the 2D plotter, and measure the magnetic field vector 100 times at each point. Fig. 20 shows the magnitude and direction of the magnetic field at each point. Fig. 20 agrees well with Fig. 6, which is obtained by simulation.

Fig. 21 shows the relationship between r_0, which is defined in Section IV-D, and the magnitude of the measured magnetic field. Fig. 21 indicates that the magnitude of the magnetic field is proportional to r_0^{-3}, which is already observed in Fig. 15 with the numerical simulation. Fig. 22 shows the relationship between θ and ξ and also indicates that ξ can be approximated by a cubic polynomial expression of θ. This relationship between θ and ξ also agrees well with the simulation result in Fig. 16.

These measurement results in this section support the proposed localization method established by simulation in Section IV. Also, Section V-B confirms that we can estimate

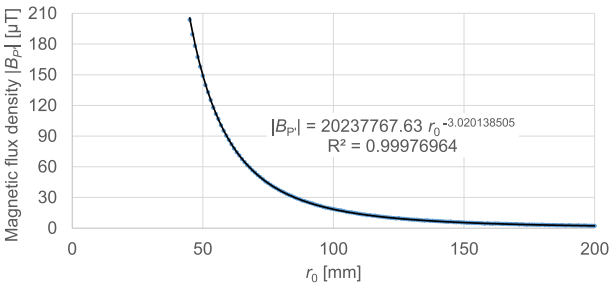

Fig. 21. Relationship between the measured magnitude of magnetic field and the value of r_0.

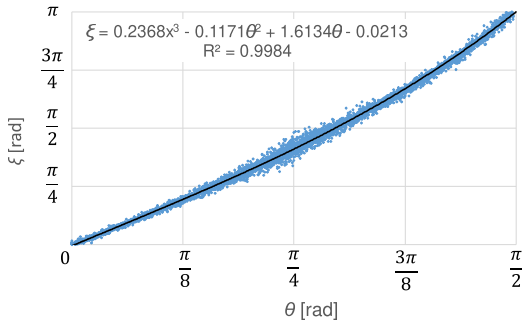

Fig. 22. Relationship between the measured ξ and θ .

the posture accurately. In addition to these, the altitude estimation is also possible since the anchor coil used in our experiment is axially symmetrical and generated magnetic field must be axially symmetrical to z axis. Consequently, we can perform 3D localization with the actual sensor node and equations in Section IV.

D. Localization Result

We perform 3D localization in the range of 150 mm × 150 mm × 150 mm with a step of 50 mm. To mitigate the effect of the geomagnetic sensor noise, each localization utilizes the average of 10 samples. In this case, the system can estimate the sensor position two times per second including the latency of the power switching of the anchor coil. Fig. 23 shows the 3D localization result, where the average of 100 localization results is plotted at each point. Fig. 23 indicates that the proposed single anchor coil based localization method can achieve high localization accuracy with a maximum error of 6.5 mm.

The proposed method aims at 3D localization, but when it is applied to 2D localization, even higher accuracy can be attained. The reason of this accuracy improvement will be discussed in Section VI-B and hence this section only focuses on the localization result itself. Fig. 24 shows the 2D localization result on the yz plane. Each circle denotes the standard deviation of the localization result at the corresponding position. We can see that the localization error and standard deviation become larger when the anchor-sensor distance becomes longer. Fig. 25 shows the relationship between the localization distance and localization error for 2D and 3D cases. The proposed method estimates 2D position with the maximum error of 1mm in the range of 125 mm and the maximum error of 3mm in the range of 250 mm,

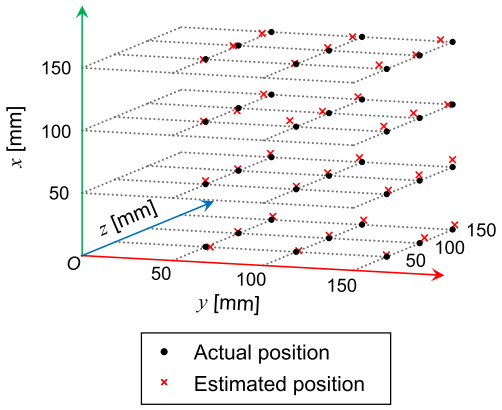

Fig. 23. 3D localization result.

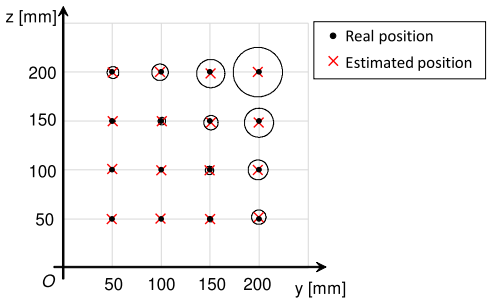

Fig. 24. 2D localization result. Each circle shows the standard deviation of the localization result at each position.

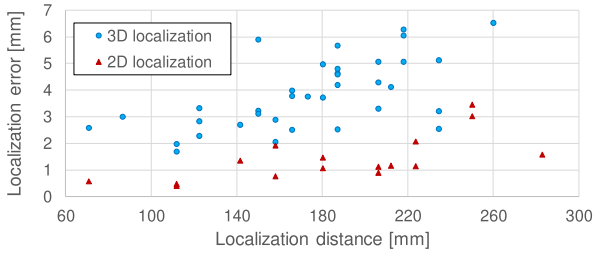

Fig. 25. Relationship between localization distance and error.

whereas in 3D case the maximum error is 3.5 mm in the range of 125 mm and 6.5 mm in the range of 250 mm, respectively. The accuracy improvement in 2D localization will be further discussed in Section VI-B.

E. Localization With Non-Ferrous Metallic Obstacle

Conventional AC magnetic field based localization methods, as we explained in Section II, suffer from the interference from metallic obstacles seriously. Our DC magnetic field based method, on the other hand, can work in the environment that contains almost all kinds of metallic obstacles except ferrous material since DC magnetic field can penetrate non-ferrous metallic obstacles. This section evaluates the performance of the proposed localization method in the environment with a non-ferrous metallic plate.

The experimental environment is depicted in Fig. 26. We install an aluminum plate whose thickness is 4 mm in parallel to the xz plane and set the origin-to-plate distance to 25 mm.

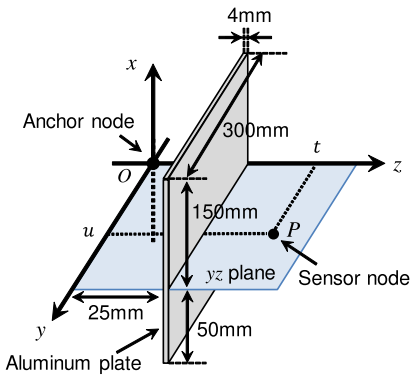

Fig. 26. Localization experimentation with an aluminum plate.

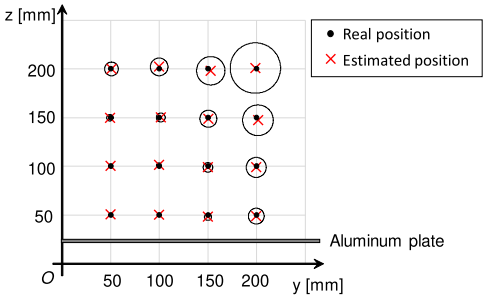

Fig. 27. 2D localization result with an aluminum plate. Each circle shows the standard deviation of the localization result at each position.

Fig. 27 shows the 2D localization result, and it is almost identical with Fig. 24 while the existence of metallic plate is different. We confirm that non-ferrous metallic obstacle does not disturb the proposed localization method.

VI. Discussion

In this section, we discuss further details about the performance of the proposed localization method. Section VI-A discusses the error caused by Eq. (17) that approximates the contour line. Section VI-B explains the reason for the difference of localization error between 2D and 3D localization in Fig. 25. Section VI-C discusses factors that determine the coverage area of the localization method and introduces two methods to expand the coverage area. Section VI-D experimentally performs coverage area expansion with multiple anchor coil. Section VI-E shows a comparison with related works.

A. Approximation Error of Contour Lines

As we discussed in Section IV, the proposed localization method consists of four steps: posture estimation, altitude estimation, distance estimation, and angle estimation. In the distance estimation step of Section IV-D, we introduced approximation equation Eq. (17) to simplify the calculation. Here in this section, we discuss the error induced by this approximation.

Fig. 28 shows the relationship between the localization distance and approximation error in the region of 0 [mm]$\leq y \leq$ 200 [mm], 0 [mm] $\leq z \leq$ 200 [mm] on yz plane. Fig. 28 indicates that the approximation error is less than 2.1 mm at the maximum, and therefore it would not be

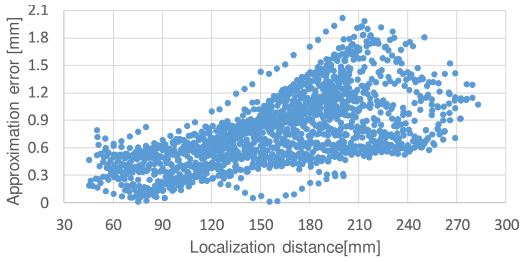

Fig. 28. Error induced by contour line approximation of Eq. (17).

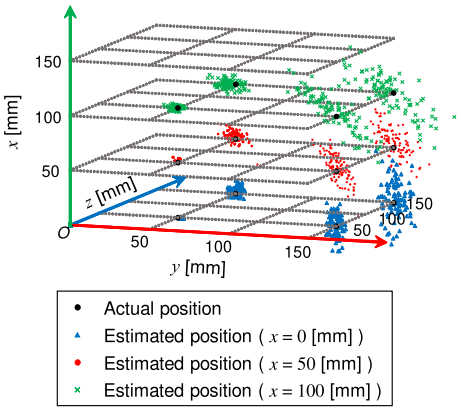

Fig. 29. Distributions of localized points.

a serious problem. Even when the approximation error observed in Fig. 28 is not acceptable in particular applications, the error can be eliminated by using LUT instead of Eq. (17).

The approximate equation of Eq. (17) requires that the sensor position should be distant enough from the anchor coil. When the sensor is located in the vicinity of the anchor coil, the approximation accuracy degrades. However, LUT-based method can handle such a vicinity region. Note that our localization method generates LUT with numerical simulation based on Eq. (1), and hence the system does not require any site survey even when utilizing LUT.

B. Analysis of Localization Error

This section analyzes the localization error and discusses the difference of the localization error between 2D and 3D localization observed in Section V-D. Fig. 29 shows the spatial distribution of several localized point. Fig. 29 indicates that the localization errors tend to spread in λ-direction. Let us explain the reason why this phenomenon occurs.

As we discussed in Section III, x-direction component of the generated magnetic field in yz plane is always zero. Therefore, λ-direction component of magnetic field must be zero at any point since the anchor coil has the axially symmetrical structure to z axis. The altitude estimation step, which is explained in Section IV-C, is based on the assumption that λ-direction component of magnetic field is zero. Hence, the accuracy of the altitude estimation is severely degraded when the λ-direction component of the measured magnetic field is non-zero because of the noise of the geomagnetic sensor. In 2D localization, we do not have to perform altitude estimation since the altitude of the sensor node is already known, and that is why 2D localization can achieve higher accuracy than 3D localization that requires altitude estimation.

TABLE I
COMPARISON WITH RELATED WORK

	[3]	[15]	[14]	This work
Method	Wifi	AC mag. field	DC mag. field	DC mag. field
Coverage area	Dozens of meter	Dozens of centimeter	Dozens of meter	Scalable (Coil diameter $\times$ 10)
Single anchor	–	Yes	No	Yes
Site survey	Necessary	Unnecessary	Necessary	Unnecessary
Sensor volume	below 1 cm^3	over 10 cm^3	below 1 cm^3	below 1 cm^3
Localization w/ non-ferrous metal	Yes	No	Yes	Yes
Localization error [cm]	150	0.11	100	0.65@25cm, 14.7@330cm

C. Relationship Between Coil Parameters and Coverage Area

This section explains factors that determine the size of coverage area and then examines two approaches for coverage area expansion. The localizable distance depends on the magnitude of the magnetic field generated by the anchor coil. Let us discuss the dependence of magnitude of the magnetic field on coil parameters. For simplifying the discussion, we approximate Eq. (1) with Eq. (25) supposing r and b satisfy the relationship of $r^2 \gg b^2$ [16].

$$\mathbf{B} = \frac{\mu_0 I b^2}{4r^3} \left(\mathbf{e}_r 2\cos\theta + \mathbf{e}_\theta \sin\theta\right). \tag{25}$$

Eq. (25) tells that I and b, which denote the amount of current injected to the anchor coil and the radius of the anchor coil, respectively, are key factors determining the magnitude of the generated magnetic field. We investigate which factor is more influential and then more important in the localization system design.

First, we focus on an increase in the amount of current. Eq. (25) shows that the localizable distance r is proportional to $I^{1/3}$ when $|B|$ is fixed. Therefore, increasing the current is not so efficient since we have to increase the current eight times for doubling the localizable distance.

Second, we investigate the diameter of the coil. Eq. (25) indicates that r is proportional to $b^{2/3}$, which is better than $I^{1/3}$. Also, we can easily increase the winding number of the coil when we enlarge the diameter of the coil. The winding number of the coil N significantly affects the magnitude of the magnetic field and localizable area since $|B| \propto N$. Hence, the strategy of enlarging the diameter and increasing the winding number of the coil should be considered first when the localizable distance expansion is demanded.

D. Coverage Area Expansion With Multiple Anchor Coils

Section V has confirmed that the proposed method is usable for table-top applications. In this section, we expand the coverage area aiming at room-scale applications using two approaches; enlarging the anchor coil and increasing the number of anchor coils.

Conventional multi-anchor based localization techniques require that the positions of all anchor nodes be measured beforehand, and consequently the installation cost is high. However, the proposed method does not require premeasurement for the second and later anchor nodes since each anchor node can estimate its own position due to the following reason. As we explained with Fig. 8 in Section IV, each anchor node is equipped with not only the localization coil but also the geomagnetic sensor. Therefore, each anchor node can sense the magnetic field generated by the previously installed anchor coil in the system, and then it can localize itself.

For evaluating the performance of the multi-anchor based localization, we install the relatively large anchor coil whose size is ϕ135 mm $\times$140 mm. Thanks to the size increase, the coverage area for a single anchor coil expands into 1.5 m $\times$ 1.5 m. First, we install Anchor #1 at the origin of the system as shown in Fig. 30. Then, we install Anchor #2 at the position of $y = 0.03000$ [m] and $z = 1.520$ [m]. In this case, the self-localization function estimated the location of $y = 0.0$ [m] and $z = 1.5$ [m]. Anchor #1 and Anchor #2 generate magnetic field in time-division manner to avoid the superposition of the magnetic field. Fig. 30 shows the measurement result with these two anchor coils and circles drawn around the localized point shows the standard deviation. The localization with Anchor #1 achieves the maximum error of 9.93 cm in the range of 2.1 m. Beyond this area, Anchor #2 is responsible for the localization, and the system estimates the position with the maximum error of 14.7 cm. In this way, the coverage area is extended by Anchor #2. Here, the localization with Anchor #2 involves larger localization error than that with Anchor #1, because Anchor #2 localizes itself with the magnetic field generated by Anchor #1, and hence the position of the Anchor #2 already includes localization error of 3.62 cm.

Finally, we mention the scalability of the time-division based method. As Eq. (25) shows, the magnitude of the DC magnetic field generated by the anchor coil is inversely proportional to the cube of the distance. Therefore, the magnetic field generated by the anchor coil decays quickly and the two anchor coils which are installed apart each other can share the radiating time. Hence, the time slot for each anchor node will not be too small and the scalability of the proposed system is sustained.

E. Comparison With Related Works

Table I shows the comparison with related works indicating that the method proposed in [15] also achieves the localization with a single anchor coil. On the other hand, the method proposed in [15] is affected by the non-ferrous metal material since it uses AC magnetic field. Also, the sensor volume is relatively large, which is not suitable for portable application.

Sensor nodes used in localization methods proposed in [3] and [14] are both small and suitable for compact application. However, the method proposed in [3] requires the site survey of Wifi singal, and hence the installation cost is relatively high. The method proposed in [14] does not require the site survey for small area localization, but it requires multiple anchor nodes and the installation cost is still high. Also for expanding

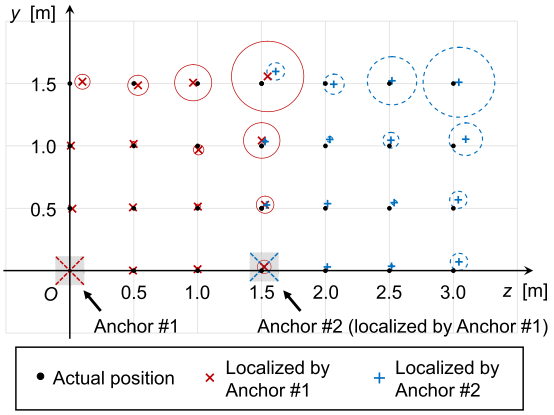

Fig. 30. Room-scale localization result with multiple anchor coils.

the localizible area, the system in [14] requires the site survey, and hence the installation cost becomes much higher according to the localizable area expansion.

From Table I, we can see that the proposed method is scalable and robust to non-ferrous material even with the single anchor coil while achieving high accuracy compared to other related works. For the applications that necessitate small-volume sensor and could have non-ferrous material nearby, the proposed localization method is the sole solution.

VII. Conclusion

We proposed a DC magnetic field based robust and scalable localization method with single anchor coil. Our localization system can reduce the installation cost significantly since our method does not require any site survey or multiple anchor nodes. We evaluated the feasibility and the performance with both numerical simulation and hardware measurement. For the tabletop-scale small area localization, the measurement result showed that the proposed localization method could achieve the maximum localization error of 3.5mm in the range of 125 mm from the anchor coil, and the maximum error of 6.5 mm in the range of 250 mm, respectively. When we installed multiple large coils for room-scale localization, the system could estimate the sensor position with the maximum error of 14.7 cm in the range of 3.3 m from the anchor coil even when the second anchor coil localizes its own position. The measurement result also indicated that the proposed localization method could work in the environment with non-ferrous metallic material since DC magnetic field can penetrate almost all kind of metallic material unlike the conventional AC magnetic field based method.

References

[1] L. Atzori, A. Iera, and G. Morabito, "The Internet of Things: A survey," *Comput. Netw.*, vol. 54, no. 15, pp. 2787–2805, Oct. 2010.
[2] G. Fortino, A. Guerrieri, G. M. O'Hare, and A. Ruzzelli, "A flexible building management framework based on wireless sensor and actuator networks," *J. Netw. Comput. Appl.*, vol. 35, no. 6, pp. 1934–1952, 2012.
[3] K. Lin, M. Chen, J. Deng, M. M. Hassan, and G. Fortino, "Enhanced fingerprinting and trajectory prediction for IoT localization in smart buildings," *IEEE Trans. Autom. Sci. Eng.*, vol. 13, no. 3, pp. 1294–1307, Jul. 2016.
[4] H.-J. Chu, G.-J. Tsai, K.-W. Chiang, and T.-T. Duong, "GPS/MEMS ins data fusion and map matching in urban areas," *Sensors*, vol. 13, no. 9, pp. 11280–11288, 2013.
[5] H. Liu, H. Darabi, P. Banerjee, and J. Liu, "Survey of wireless indoor positioning techniques and systems," *IEEE Trans. Syst., Man, Cybern. C, Appl. Rev.*, vol. 37, no. 6, pp. 1067–1080, Nov. 2007.
[6] F.-J. Zhu, Z.-H. Wei, B.-J. Hu, J.-G. Chen, and Z.-M. Guo, "Analysis of indoor positioning approaches based on active rfid," in *Proc. 5th Int. Conf. Wireless Commun., Netw. Mobile Comput.*, Sep. 2009, pp. 1–4.
[7] S. He and S.-H. G. Chan, "Wi-Fi fingerprint-based indoor positioning: Recent advances and comparisons," *IEEE Commun. Surveys Tuts.*, vol. 18, no. 1, pp. 466–490, Jan. 2015.
[8] C. Yang and H.-R. Shao, "WiFi-based indoor positioning," *IEEE Commun. Mag.*, vol. 53, no. 3, pp. 150–157, Mar. 2015.
[9] C. Wu, Z. Yang, Y. Liu, and W. Xi, "WILL: Wireless indoor localization without site survey," *IEEE Trans. Parallel Distrib. Syst.*, vol. 24, no. 4, pp. 839–848, Apr. 2013.
[10] F. Zafari, I. Papapanagiotou, and K. Christidis, "Microlocation for Internet-of-Things-equipped smart buildings," *IEEE Internet Things J.*, vol. 3, no. 1, pp. 96–112, Feb. 2016.
[11] R. Figueiredo, A. Dehban, A. Bernardino, J. Santos-Victor, and H. Araújo, "Shape-based attention for identification and localization of cylindrical objects," in *Proc. IEEE Int. Conf. Develop. Learn. Epigenetic Robot. (ICDL-EpiRob)*, vol. 18, Sep. 2017, p. 21.
[12] V. Pasku *et al.*, "Magnetic field-based positioning systems," *IEEE Commun. Surveys Tuts.*, vol. 19, no. 3, pp. 2003–2017, 3rd Quart., 2017.
[13] G. De Angelis *et al.*, "An indoor AC magnetic positioning system," *IEEE Trans. Instrum. Meas.*, vol. 64, no. 5, pp. 1267–1275, May 2015.
[14] J. Blankenbach, A. Norrdine, and H. Hellmers, "A robust and precise 3d indoor positioning system for harsh environments," in *Proc. Int. Conf. Indoor Positioning Indoor Navigat. (IPIN)*, Nov. 2012, pp. 1–8.
[15] S. Song, C. Hu, B. Li, X. Li, and M. Q.-H. Meng, "An electromagnetic localization and orientation method based on rotating magnetic dipole," *IEEE Trans. Magn.*, vol. 49, no. 3, pp. 1274–1277, Mar. 2013.
[16] D. K. Cheng, *Fundamentals of Engineering Electromagnetics*. New York, NY, USA: Addison-Wesley, 1993.

Ryo Shirai (Student Member, IEEE) received the B.E. and M.E. degrees in information systems engineering from Osaka University, Suita, Japan, in 2016 and 2018, respectively, where he is currently pursuing the Ph.D. degree in information science and technology. He has been a Research Fellow with the Japan Society for the Promotion of Science (JSPS) since 2019. His current research interests include analog circuit design, embedded systems, and sensor systems.

Masanori Hashimoto (Senior Member, IEEE) received the B.E., M.E., and Ph.D. degrees in communications and computer engineering from Kyoto University, Kyoto, Japan, in 1997, 1999, and 2001, respectively. He is currently a Professor with the Department of Information Systems Engineering, Graduate School of Information Science and Technology, Osaka University, Suita, Japan. His current research interests include the design for manufacturability and reliability, timing and power integrity analysis, reconfigurable computing, soft error characterization, and low-power circuit design. Dr. Hashimoto was a recipient of the Best Paper Award from Asia and South Pacific Design Automation Conference in 2004 and the Best Paper Award of the IEICE Transactions in 2016. He was on the Technical Program Committee of international conferences, including Design Automation Conference, International Conference on Computer Aided Design, International Test Conference, Symposium on VLSI Circuits, ASP-DAC, and DATE. He serves/served as an Associate Editor for the IEEE Transactions on Very Large Scale Integration, the IEEE Transactions on Circuits and Systems I, *ACM Transactions on Design Automation of Electronic Systems*, and *Microelectronics Reliability* (Elsevier).